

MEASUREMENT OF THE ANTIHYDROGEN HYPERFINE STRUCTURE

Letter of Intent for AD

E. Widmann¹, J. Eades¹, R.S. Hayano¹, T. Ishikawa¹, W. Pirkel¹, M. Hori², Y. Yamazaki^{3,4}, A. Mohri³, T. Yamazaki⁵, D. Horváth⁶, B. Juhász⁷, E. Takács⁷

- 1) *Department of Physics, University of Tokyo, 7-3-1- Hongo, Bunkyo-ku, Tokyo 113-0033, Japan*
- 2) *CERN, EP Division, Ch-1211 Geneva 23*
- 3) *Institute of Physics, University of Tokyo, Komaba, Meguro-ku, Tokyo 153-8902, Japan*
- 4) *Atomic Physics Laboratory, RIKEN, Wako 351-01, Japan*
- 5) *RI Beam Science Laboratory, RIKEN, Wako, Saitama 351-0198, Japan*
- 6) *KFKI Research Institute for Particle and Nuclear Physics, H-1525 Budapest, Hungary*
- 7) *Department of Experimental Physics, Lajos Kossuth University, H-4001 Debrecen, Hungary*

ASACUSA Collaboration

Contents

1	Executive Summary	3
2	Introduction	4
2.1	Hyperfine structure in hydrogen and antihydrogen	4
2.2	CPT invariance and atomic spectroscopy	4
2.2.1	Interpreting particle-antiparticle comparisons	4
2.2.2	The 1S-2S frequency for hydrogen and antihydrogen	4
2.2.3	The classical Lamb shift for hydrogen and antihydrogen	6
2.2.4	The hyperfine frequency for hydrogen and antihydrogen	6
2.3	Atomic antihydrogen beam experiments	6
3	Physics of the ground-state hyperfine structure and CPT violation	7
4	A theoretical model for CPT violation	8
5	Experimental considerations	11
5.1	Essential characteristics of formed antihydrogen	11
5.2	The antihydrogen beam line	11
5.3	Velocity distribution of antihydrogen atoms in the beam	13
5.4	Antihydrogen beam transport in sextupole fields	13
5.5	Microwave resonance apparatus	15
5.6	Resonance line shape and achievable resolution	15
5.7	Antihydrogen detection	16
6	Antihydrogen Production	17
6.1	$\bar{\text{H}}$ production in nested Penning traps in a split solenoid magnet	17
6.2	$\bar{\text{H}}$ production in radio frequency Paul traps	21
6.2.1	Experimental apparatus and methods	22
6.2.2	$\bar{\text{H}}$ formation procedure	24
6.2.3	Feasibility tests to be done at CERN and their requirements	25
6.3	Synthesis of a polarized $\bar{\text{H}}$ beam with a cusp trap	26
7	Positron production	28
8	Technical milestones	29

1 Executive Summary

The frequency ν_{HF} of the ground state hyperfine structure (GS-HFS) of the hydrogen atom is, like its 1S-2S frequency, one of the most precisely measured fundamental quantities in physics. This extremely high precision is the end point of a classic series of experiments which began in the 1930's with relatively simple atomic beam experiments, and culminated with maser experiments in the early 1970s which ultimately achieved a relative precision of order 10^{-12} . In this Letter of Intent we discuss a series of microwave experiments on the GS-HFS of antihydrogen, $\bar{\text{H}}$, which parallels this historical development from simple to complex experimentation, and which we plan to present as a full proposal when our current technical feasibility studies are complete.

We intend to recombine antihydrogen atoms from positrons and antiprotons captured in either a nested Penning trap, a Paul trap, or a cusp trap. The antihydrogen atoms will emerge from the formation region as an atomic beam, and will traverse a pair of sextupole magnets after a short field-free region. The first sextupole will select the spin and velocity of the $(F, M) = (1, 1)$ and $(1, 0)$ "low-field seeking" antihydrogen atoms states while the second one analyzes the spin state of the transmitted antihydrogen atoms. A microwave cavity introduced between the sextupoles will induce spin flip transitions $(F, M) = (1, 1) \rightarrow (0, 0)$ and $(1, 0) \rightarrow (0, 0)$, giving a value of ν_{HF} with precision $\Delta\nu_{\text{HF}}/\nu_{\text{HF}} \sim 10^{-6}$ or better. Since the precision is limited by the transit time of $\bar{\text{H}}$ atoms in the resonance cavity, ever higher precision will be attained as the recombination condition of $\bar{\text{H}}$ is improved. If the already published production rates of $\bar{\text{H}}$ are scaled by the factor 100 higher deceleration efficiency of the ASACUSA RFQD, reasonable count rates of 1 event per minute can be expected at the $\bar{\text{H}}$ detector.

For the production of ground-state antihydrogen atoms, we are currently evaluating three possible scenarios. The method already demonstrated at the AD in 2002, nested traps, is a possible but not optimal solution because the large size of the particle clouds requires the use of very large sextupole magnets to reduce the effect of aberration. A much better solution in terms of access and size of particle clouds is to use Paul traps. The simultaneous trapping of electrons or positrons with opposite charge ions in a pure Paul trap has never been experimentally achieved, and it will need a dedicated R&D program. We plan to use the duoplasmatron proton source of AB division to produce a low-energy proton beam with the parameters of our RFQD, and demonstrate trapping and cooling in a catching Paul trap, and transfer of protons from it to the recombination Paul trap. As a next step, the simultaneous trapping of protons and electrons will be investigated. For the construction of the superconducting RF traps, we will need to consult with CERN experts on cryogenics and superconducting cavities, and use some of the CERN workshop and laboratory facilities in manufacturing some of the technically difficult parts of the RF Paul traps. The third approach is the use of a cusp trap (a magnetic-bottle like structure well-known in plasma physics), which has the advantage of producing a polarized $\bar{\text{H}}$ beam. The cusp trap is currently being built and will be tested with protons and electrons at the Atomic Physics Laboratory at RIKEN.

We plan to evaluate the formation schemes until the end of 2004, install all equipment at the AD during the shutdown 2005, test antiproton and positron injection and cooling during 2006 and 2007, and start measurements with the antihydrogen beam line in the latter half of 2007.

2 Introduction

2.1 Hyperfine structure in hydrogen and antihydrogen

Since the ground state of antihydrogen has infinite lifetime, its high precision spectroscopy will give unprecedented accuracies in terms of CPT symmetry tests. In the case of hydrogen, the ground-state hyperfine splitting frequency ν_{HF} has been measured in a classic series of experiments which began in the 1930's with relatively simple atomic beam experiments, and culminated with maser experiments in the early 1970s which ultimately achieved a relative precision of order 10^{-12} . For the antihydrogen atom, a measurement of ν_{HF} with precision equal to that achieved in the hydrogen case some fifty years ago would constitute a commensurately precise test of CPT symmetry. It may also be interpreted in terms of the gravitational interaction of antimatter.

To the leading order, the GS-HFS of antihydrogen is proportional to the spin magnetic moment of the antiproton, $\vec{\mu}_{\bar{p}}$, which is experimentally known only at the level of 0.3%. Below the level of several ppm accuracy, ν_{HF} also depends on the electric and magnetic form factors of the antiproton (cf. section 3). The measurements of $\nu_{\text{HF}}(\bar{\text{H}})$ to a relative accuracy of better than 10^{-6} as discussed in this letter will therefore yield an improvement of the value of $\vec{\mu}_{\bar{p}}$ by three orders of magnitude, and give some insight into the structure of the antiproton. Furthermore, the only existing phenomenological extension of the standard model that includes CPT violations (that of Kostelecky's group, see section 4) predicts that CPT violation in the 1S–2S transition is cancelled in first order, while for the hyperfine structure it is a leading-order effect.

2.2 CPT invariance and atomic spectroscopy

2.2.1 Interpreting particle-antiparticle comparisons

In Table 1 and Fig. 1 we summarize the presently known physical quantities for the proton, the electron and the hydrogen atom, together with the precision of the theoretical values. Also shown are presently known CPT-invariant properties, which we define for a general case X as:

$$\Delta_{CPT}(X) = \frac{X(\text{antiparticle}) - X(\text{particle})}{X(\text{particle})}. \quad (1)$$

Although relative precisions like those of equation 1 are dimensionless, care must be taken in interpreting them. First, the scale of X is ambiguous in definition. Thus, Δ_{CPT} of the 1S *binding energy* of hydrogen must have the same significance in terms of CPT invariance as Δ_{CPT} of the *total energy including the rest mass* of the 1S state of hydrogen, but differs from it in absolute magnitude by 8 orders. Second, symmetry violations of all kinds depend on the nature of the physical observables involved. For instance, parity violation dominates only the weak interaction world and CP violation occurs only in the neutral K and B mesons. Nobody knows in which physical quantities CPT violation may appear.

2.2.2 The 1S-2S frequency for hydrogen and antihydrogen

The 1S-2S transition energy is primarily determined by the electron or positron Rydberg constant, as this is directly proportional to the reduced electron-proton (positron-antiproton) mass. Thus (as Fig. 1 illustrates) the positron mass determines the first significant figure of $\nu_{1\text{S}-2\text{S}}$ for antihydrogen while the antiproton mass only begins to take effect at the fourth place. The *theoretical uncertainty* for the hydrogen atom is in the eleventh place [2, 3] and is due to uncertainty of $\sqrt{\langle R_p^2 \rangle} = 0.862 \pm 0.012$ fm [13] in the proton radius. In this sense, eleventh place precision in determining

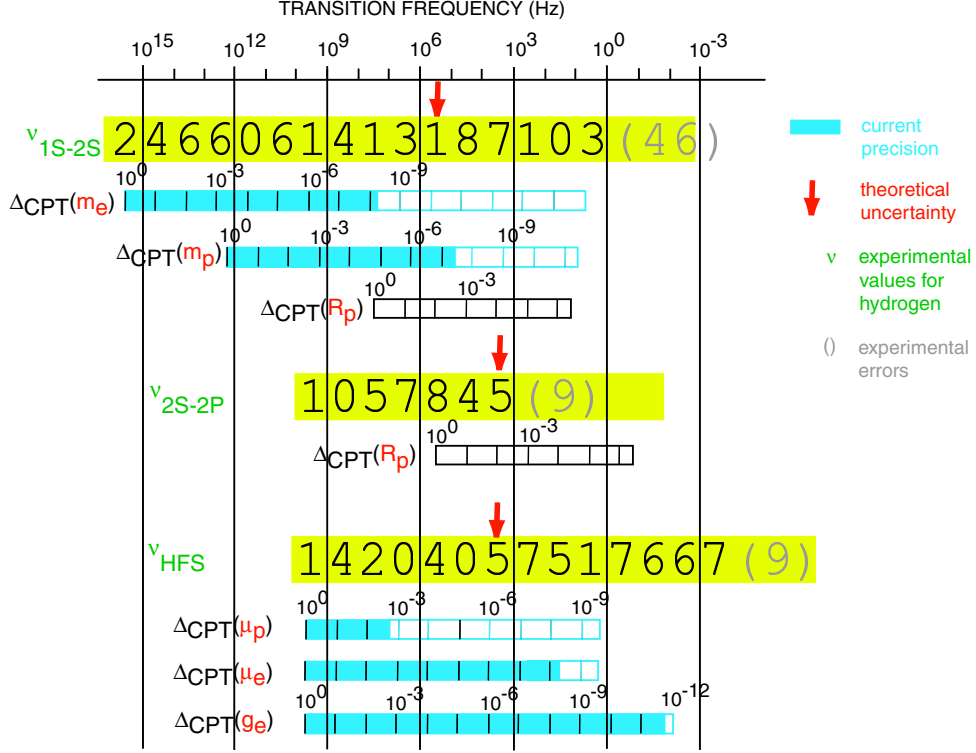


Figure 1: Three experimental values (large numerical letters) of the 1S-2S transition frequency, 2S-2P Lamb shift and the 1S hyperfine frequency of hydrogen are presented together with the theoretical uncertainties. Known information on CPT symmetry is also shown (cf. Table 1).

Table 1: Measured quantities of proton, electron, and hydrogen. m_e : electron mass, m_p : proton mass, R_p : proton radius, μ_e : electron magnetic moment, μ_p proton magnetic moment, g_e electron g-factor. δ_{exp} and δ_{th} denote the experimental or theoretical error. * difference between theory and experiment $(\nu_{\text{th}} - \nu_{\text{exp}})/\nu_{\text{exp}}$. ** the accuracy of the electron magnetic moment is determined by the accuracy of the electron mass.

Measured quantities of hydrogen					
quantity	exp. value (Hz)	δ_{exp}/ν	ref.	δ_{th}/ν	ref.
ν_{1S-2S}	2 466 061 413 187 103(46)	1.7×10^{-14}	[1]	1×10^{-11}	[2, 3]
ν_{2S-2P}	$1\ 057\ 845(9) \times 10^3$	8.5×10^{-7}	[4]	8×10^{-6}	[5]
ν_{HFS}	1 420 405 751.7667(9)	6.3×10^{-13}	[6, 7]	$(3.5 \pm 0.9) \times 10^{-6}$ *	[8]
Measured CPT quantities					
quantity	value		ref.		
$\Delta_{\text{CPT}}(m_e)$	8×10^{-9}		[9]		
$\Delta_{\text{CPT}}(m_p)$	6×10^{-8}		[10]		
$\Delta_{\text{CPT}}(R_p)$	—				
$\Delta_{\text{CPT}}(\mu_p)$	$(-2.6 \pm 2.9) \times 10^{-3}$		[11]		
$\Delta_{\text{CPT}}(\mu_e)$	8×10^{-9}	**			
$\Delta_{\text{CPT}}(g_e)$	$(-0.5 \pm 2.1) \times 10^{-12}$		[12]		

the hydrogen and antihydrogen 1S-2S energies yields primarily information on the proton and antiproton charge distributions.

2.2.3 The classical Lamb shift for hydrogen and antihydrogen

The frequency interval ν_{2S-2P} between the $2S_{1/2}$ and $2P_{1/2}$ states of hydrogen has played an important role in the development of Quantum Electrodynamics, since it exclusively originates from QED effects. The experimental precision for ν_{2S-2P} is however rather limited due to the short lifetime of the $2P_{1/2}$ state of $\tau_{2P_{1/2}} = 1.6$ ns corresponding to a natural linewidth of 100 MHz, so that its use for high-precision CPT tests is not very promising.

2.2.4 The hyperfine frequency for hydrogen and antihydrogen

The 1S ground state of hydrogen is split due to the interaction of electron spin \vec{S}_e and proton spin \vec{S}_p according to $\vec{F} = \vec{S}_e + \vec{S}_p$ with quantum numbers $F = 0, 1$ (total spin) and $M = -1, 0, 1$ (projection of F onto the magnetic field axis). The hyperfine splitting between the $F = 0$ and $F = 1$ states of the hydrogen and antihydrogen atoms is directly proportional to both the electron(positron) and proton(antiproton) spin magnetic moments. As with the 1S-2S transition, it is extremely well-known empirically for hydrogen. The impact of this on quantum physics at every stage of its development has been considerable, as Ramsey's extremely useful and informative review [14] demonstrates. These studies date back to the early 1930's, when Rabi [15–17] made a simple Stern-Gerlach beamline of inhomogeneous magnetic fields used as spin-state selectors, through which hydrogen atoms were transported. Even from such a primitive experiment a value of the hyperfine coupling constant, $\nu_{\text{HF}} = 1421.3 \pm 0.2$ MHz, could be deduced. A similar experimental feat should easily be reproducible with an antihydrogen beam.

The advent of magnetic resonance methods saw determinations of the hyperfine splitting of the hydrogen ground state via microwave-induced transitions, first by Nafe and Nelson [18] and later by Prodell and Kusch [19]. The precision attained by the first resonance experiment ($\nu_{\text{HF}} = 1420.410 \pm 0.002$ MHz) was already impressive, surpassing even the present-day theoretical uncertainty in the seventh place (Fig. 1). In this new phase, the "Stern-Gerlach beamline" was supplemented by a resonant cavity inserted between the magnets. The transit time through this cavity then became the factor that set an intrinsic, but nevertheless considerably improved, limit on the resonance width. In the context of these experiments, atomic beams can usefully be thought of as a kind of two-dimensional trap, whose confinement time is equal to the beam transit time. When it became possible to observe hydrogen atoms for times of order 10 seconds in a maser cavity, the precision increased accordingly, [20], and it is in such experiments that the best value of ν_{HF} to date [6, 7, 14] :

$$\nu_{\text{HF}} = 1\,420\,405\,751.766\,7 \pm 0.0009 \text{ Hz} \tag{2}$$

was obtained.

2.3 Atomic antihydrogen beam experiments

Maser conditions are probably unobtainable with antihydrogen at the moment, since the spin-state selected atoms are not trapped in the maser cavity, but make many wall collisions before finding their way out through their entrance aperture. Attempts to measure ν_{HF} by microwave spectroscopy in neutral-atom traps are limited in accuracy due to the inhomogeneous magnetic field used for trapping, and the finite temperature distribution of the trapped atoms. E.g. in a

typical neutral-atom trap used for hydrogen spectroscopy [21], the atoms will experience Zeeman level shifts due to their thermal motion. So far experiments on RF-spectroscopy of trapped neutral atoms have not been able to achieve high precision, but only to extract the temperature distribution of atoms, even though these atoms had a temperature as small as 60 mK [22, 23].

We therefore believe that experiments carried out with an antihydrogen beam of energy corresponding to about 10 K has an enormous, but yet untapped potential for testing CPT-symmetry. Atomic beams sacrifice the long storage times of neutral atom traps in favour of simplicity of construction, operation, and experimental complexity. To judge by the number of fundamental physical quantities that have been determined to high precision in such beams, this tradeoff has frequently been worthwhile. These include not only the HFS frequency in hydrogen and its above-cited concomitant, the proton magnetic moment, but also the fine structure constant itself (from fine and hyperfine structure measurements of one- and two-electron atoms), the Lamb shift, the equality of proton and electron charges to one part in 10^{18} and upper limits on the electric quadrupole moment of the electron and proton.

Seen in this perspective, experiments to measure the hyperfine structure appear not only feasible - the initial ones might have been carried out in the 1930s had antihydrogen beams been available then - but also logically and empirically meaningful. Thus, without pushing microwave and magnet technology to unreasonable limits, we can expect to parallel with antihydrogen the historical development of the hydrogen case, starting from a simple Stern-Gerlach experiment and proceeding to microwave resonance experiments, with better and better values for the antihydrogen hyperfine frequency ν_{HF} emerging at each stage. We base our intention to measure the hyperfine structure of the ground state of the antihydrogen at the AD on these experimental grounds. Section 3 describes in more detail the ground-state hyperfine structure, and section 4 gives some additional theoretical material on CPT violation. In Section 5 we develop our experimental strategy to measure the hyperfine structure in an atomic beam of antihydrogen atoms, and in section 6 we discuss the possible scenarios for producing cold $\bar{\text{H}}$ atoms. Section 7 deals with positron production schemes, and section 8 describes technical milestones.

3 Physics of the ground-state hyperfine structure and CPT violation

The hyperfine structure of antihydrogen provides a variety of physics implications, which are unique and qualitatively different from those given by the binding energy of antihydrogen. The hyperfine coupling frequency ν_{HF} in the hydrogen ground state is given to the leading term by the Fermi contact interaction, yielding

$$\nu_F = \frac{16}{3} \left(\frac{M_p}{M_p + m_e} \right)^3 \frac{m_e}{M_p} \frac{\mu_p}{\mu_N} \alpha^2 c Ry, \quad (3)$$

which is a direct product of the electron magnetic moment and the anomalous proton magnetic moment (M_p , m_e denote proton and electron mass, c the speed of light, α the fine structure constant, and Ry the Rydberg constant). Using the known proton magnetic moment,

$$\mu_p = 2.792\,847\,386(63) \mu_N, \quad (4)$$

with

$$\mu_N = 7.622\,591\,4 \text{ MHz/T}, \quad (5)$$

this formula yields $\nu_F = 1418.83 \text{ MHz}$, which is significantly different from the experimental value. This 1000 -ppm discrepancy led to the discovery of the anomalous electron g -factor ($g_e = 2.002$).

Even after higher-order QED corrections [2] still a significant difference between theory and experiment remained, as

$$\delta(\text{QED}) = \frac{\nu(\text{QED}) - \nu(\text{Exp})}{\nu(\text{Exp})} = 32.55(10) \text{ ppm.} \quad (6)$$

This discrepancy was accounted for by the non-relativistic magnetic size correction (Zemach correction) [2]:

$$\Delta\nu(\text{Zemach}) = \nu_{\text{F}} \frac{2Z\alpha m_e}{\pi^2} \int \frac{d^3p}{p^4} \left[\frac{G_E(p^2)G_M(p^2)}{1 + \kappa} - 1 \right], \quad (7)$$

where ν_{F} is the Fermi contact term defined in eq. (3), $G_E(p^2)$ and $G_M(p^2)$ are the electric and magnetic form factor of the proton, and κ its anomalous magnetic moment. The Zemach corrections therefore contain both the magnetic and charge distribution of the proton.

A detailed treatment of the Zemach corrections can be found in [8]. Assuming the validity of the dipole approximation, the two form factors can be correlated

$$G_E(p^2) = \frac{G_M(p^2)}{1 + \kappa} = \left(\frac{\Lambda^2}{\Lambda^2 + p^2} \right)^2 \quad (8)$$

where the Λ is related to the proton charge radius by $R_p = \sqrt{12}/\Lambda$. Whether the dipole approximation is indeed a good approximation, however, is not really clear. Integration by separation of low and high-momentum regions with various separation values, and the use of different values for R_p gives a value for the Zemach corrections of $\Delta\nu(\text{Zemach}) = -41.07(75)$ ppm [8]. With this correction, and some more recently calculated ones, the theoretical value deviates from the experimental one by [8]

$$\frac{\nu(\text{exp}) - \nu(\text{th})}{\nu(\text{exp})} = 3.5 \pm 0.9 \text{ ppm.} \quad (9)$$

A further structure effect, the proton polarizability, is only estimated to be < 4 ppm [8], of the same order than the value above. The ‘‘agreement’’ between theory and experiment is therefore only valid on a level of ~ 4 ppm. Thus, we can say that the uncertainty in the hyperfine structure reflects dominantly the electric and magnetic distribution of the proton, which is related to the origin of the proton anomalous moment, a current topic of particle-nuclear physics.

The hyperfine structure of antihydrogen ($\nu_{\text{HF}}(\bar{\text{H}})$) gives unique and qualitatively different information from that given by the binding energies of antihydrogen atomic states. Historically, of course, it was the hyperfine coupling constants of hydrogen and deuterium which first indicated that the values of the proton and deuteron magnetic moments were surprisingly anomalous. A first measurement of the antihydrogen hyperfine structure will initially provide a better value for the poorly known antiproton magnetic moment ($\mu_{\bar{p}}$), the current 0.3 % relative precision of which has been obtained from the fine structure of heavy antiprotonic atoms [24]. Subsequent, more precise values of $\nu_{\text{HF}}(\bar{\text{H}})$ will yield information on the magnetic form factor of the antiproton ($G_M(\bar{p})$), etc.

4 A theoretical model for CPT violation

At what scale and in what kind of physical observables might we then find CPT violating effects and what might be their significance? As is well known, CPT violation would require the abandonment of one or more of the cherished axioms of relativistic quantum field theory, which has had

conspicuous success in all domains of particle physics. It is the fact that even so, most physicists believe that for a variety of reasons the standard model is incomplete that drives speculation about CPT-violation. For example, since several of the conditions required in the mathematical proof of the CPT theorem no longer hold in string theory, CPT violation could be used as a signature for string theory.

In recent years, the group of V.A. Kostelecky at Indiana has developed an extension to the standard model that includes both CPT as well as Lorentz-invariance violating (LIV) terms in the Lagrangian of a quantum field theory [25–29]. Although this model does not directly predict any CPT violation nor LIV, it can be used as basis to compare CPT tests in different sectors, and as a guide where to look for possible CPT violating effects. In fact, various group have already done so [30–36]. We describe this particular model below (although we do not base our proposed study of the antihydrogen hyperfine structure on it alone).

For the case of hydrogen and antihydrogen, the model [29] has the feature that CPT-violation effects might modify the triplet-singlet hyperfine structures of both hydrogen and antihydrogen, but differently. By introducing a number of CPT-violating parameters (generically denoted by a, b, c , and d below) as well as Lorentz-invariance violating (LIV) terms these authors can relate each of various physical observables to the theoretical parameters. In the hydrogen atom this adds an energy correction to states with electron and proton spin components m_J and m_I with value (m_e and m_p denote the electron and proton mass, resp.):

$$\Delta E^H(m_J, m_I) = a_0^e + a_0^p - c_{00}^e m_e - c_{00}^p m_p \quad (10)$$

$$+(-b_3^e + d_{30}^e m_e + H_{12}^e) m_J / |m_J| \quad (11)$$

$$+(-b_3^p + d_{30}^p m_p + H_{12}^p) m_I / |m_I|. \quad (12)$$

For antihydrogen, the parameters a , d , and H reverse sign. The anomalous energy terms ΔE^H and $\Delta E^{\bar{H}}$ arise from Lorentz invariance violation, among which the parameters a_0 's and b_3 's are responsible for CPT violation. Since the transition energy is a difference of two energy levels, it does not involve any of the above parameters (unless the transitions between hyperfine levels are measured in a magnetic field), making the 1S–2S transition frequency of free hydrogen and antihydrogen insensitive to the type of CPT violation described in this model. On the other hand, the hyperfine states have the following energy shifts (the indices 1 to 4 refer to the different states as shown in Fig. 2)

$$\begin{aligned} \#1 \quad (F, M) = (1, 1) : \quad & \Delta E_1^H = -b_3^e - b_3^p + d_{30}^e m_e + d_{30}^p m_p + H_{12}^e + H_{12}^p \\ \#2 \quad (F, M) = (1, 0) : \quad & \Delta E_2^H = -\cos 2\theta [b_3^e - b_3^p - d_{30}^e m_e + d_{30}^p m_p - H_{12}^e + H_{12}^p] \\ \#3 \quad (F, M) = (1, -1) : \quad & \Delta E_3^H = -\Delta E_1^H \\ \#4 \quad (F, M) = (0, 0) : \quad & \Delta E_4^H = -\Delta E_2^H, \end{aligned} \quad (13)$$

where $\cos 2\theta$ represents the mixing of the (1, 0) and (0, 0) states (the mixing angle depends on the principal quantum number n and the magnetic fields B and obeys $\tan 2\theta_n \approx (51\text{mT})/n^3 B$). In this way, the hyperfine transition frequencies are directly connected to the parameters of the spin-dependent terms.

In the presence of an external field B the $F = 1$ and $F = 0$ energy levels are split according to the Breit-Rabi formula:

$$\begin{aligned} \#1 : (F, M) = (1, 1) : \quad & E_1 = \frac{1}{4}E_0 + \frac{1}{2}(g_J + g_I)\mu_B B + \Delta E_1 \\ \#2 : (F, M) = (1, 0) : \quad & E_2 = -\frac{1}{4}E_0 + \frac{1}{2}E_0\sqrt{1+x^2} + \Delta E_2 \\ \#3 : (F, M) = (1, -1) : \quad & E_3 = \frac{1}{4}E_0 - \frac{1}{2}(g_J + g_I)\mu_B B - \Delta E_1 \\ \#4 : (F, M) = (0, 0) : \quad & E_4 = -\frac{1}{4}E_0 - \frac{1}{2}E_0\sqrt{1+x^2} - \Delta E_2, \end{aligned} \quad (14)$$

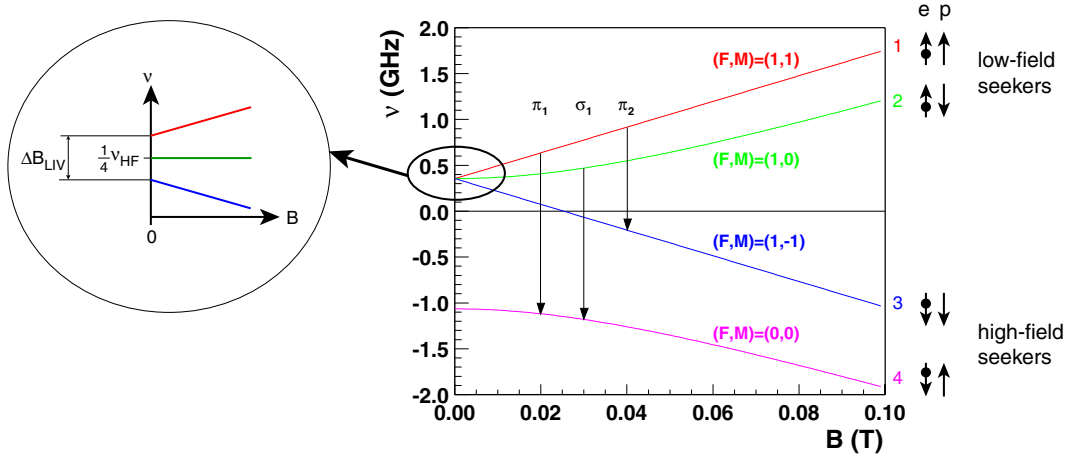


Figure 2: Right: Zeeman splitting of the ground state hyperfine levels of hydrogen (Breit-Rabi diagram). The spin alignments of electron and proton in the high-field limit, when the spins are decoupled, is shown to the right. Left: Zero-field splitting of the $F = 1$ states in the presence of a CPT violating interaction as predicted by Bluhm et al. [29].

where

$$x = \frac{B}{B_0}, \quad (15)$$

$$\text{and } B_0 = \frac{E_0}{(g_J - g_I)\mu_B \hbar} = \frac{2\pi\nu_{\text{HF}}}{(g_J - g_I)\mu_B} = 3179.7225 \text{ Gauss}. \quad (16)$$

One consequence of this model is that the degeneracy of the $F = 1$ triplet state at zero applied magnetic field (B) is lifted, giving the $(F, M) = (1, 1)$ and $(1, -1)$ states opposite energy shifts, as shown in Fig. 2. The effect is as if a very small fictitious pseudo-magnetic field

$$\Delta B_{\text{LIV}} = \frac{2\Delta E_1^{\text{H}}}{g_J \mu_B} \quad (17)$$

were present in free space. Furthermore, a part of ΔE_1^{H} depends on the CPT-violating parameters, and changes sign for $\text{H} \rightarrow \bar{\text{H}}$. For a magnitude of the CPT-violating parameters leading to $\Delta E_1^{\text{H}}/h = 1 \text{ Hz}$, ΔB_{LIV} would be 10^{-6} Gauss. The quantization axis and the direction of the hypothetical pseudo-magnetic field must then somehow be defined, perhaps with respect to the earth's rotation axis (in which case the energy shifts would be subject to diurnal variation).

CPT-violation of this kind would therefore show up as hyperfine structure anomalies to be detected by studying spin-state polarizations. Were we dealing with muonium and antimuonium, the corresponding spin polarization would be revealed by the muon decay asymmetry. In the hydrogen/antihydrogen case this possibility is obviously not available; polarization states may nevertheless be selected and analyzed by their spin-dependent deflection in inhomogeneous magnetic fields. The hyperfine transitions that can be detected under these circumstances are:

$$\begin{aligned}
\pi_1 : (F, M) = (1, 1) \rightarrow (0, 0) : \quad \nu_{14} &= \frac{1}{4}\nu_0 + \frac{1}{4\pi}(g_J + g_I)\mu_B B + \frac{1}{2}\nu_0\sqrt{1+x^2} + \frac{\Delta E_1 - \Delta E_4}{h} \\
\pi_2 : (F, M) = (1, 0) \rightarrow (1, -1) : \quad \nu_{23} &= \frac{1}{2}\nu_0 \left[-1 + \sqrt{1+x^2} \right] + \frac{1}{4\pi}(g_J + g_I)\mu_B B + \frac{\Delta E_2 - \Delta E_3}{h} \\
\sigma_1 : (F, M) = (1, 0) \rightarrow (0, 0) : \quad \nu_{24} &= \nu_0\sqrt{1+x^2} + \frac{2\Delta E_2}{h}.
\end{aligned} \tag{18}$$

The low-field seeking states (1,1) and (1,0) initially selected are converted to high-field seeking states (1,-1) and (0,0). Since the transition frequencies of all these transitions are highly dependent on the external field, only zero (or very low) field conditions are experimentally suitable for high-precision spectroscopy, Only the π_1 and σ_1 transitions can therefore be detected. Their frequencies in the limit of $B \rightarrow 0$ are:

$$\begin{aligned}
\pi_1 : (F, M) = (1, 1) \rightarrow (0, 0) : \quad \nu_{14} &= \nu_0 + \frac{1}{4\pi}(g_J + g_I)\mu_B B + \frac{\Delta E_1}{h} \\
\sigma_1 : (F, M) = (1, 0) \rightarrow (0, 0) : \quad \nu_{24} &= \nu_0.
\end{aligned} \tag{19}$$

The π_1 resonance may then show an anomaly, while the σ_1 resonance does not.

5 Experimental considerations

5.1 Essential characteristics of formed antihydrogen

Possible ways to form antihydrogen atoms from trapped antiprotons and positrons will be described in section 6. It is common to all scenarios that the atoms are no longer confined by the magnetic or RF fields and can thus escape from the formation region in all directions. Recently cold antihydrogen atoms have been produced by ATHENA [37] and ATRAP [38, 39] using nested Penning traps initially proposed by Gabrielse et al. [40]. The formed $\bar{\text{H}}$ atoms are believed to have temperatures of 4.2 or 15 K, resp., according to the cryogenic environment in which they are produced. Analogous conditions apply to the other formation methods.

For the measurement of ν_{HF} as well as $\nu_{1\text{S}-2\text{S}}$ it is necessary to form antihydrogen atoms in the ground state. While ATRAP reported mostly Rydberg-antihydrogen [38], there is some indication that ATHENA has mostly produced ground-state $\bar{\text{H}}$ from the $1/\sqrt{T}$ dependence of the formation rate [41]. This is consistent with the higher temperature used in ATHENA. It is also possible to enhance the ground-state fraction by using laser stimulated recombination [42, 43], for which access for laser beams to the formation region has to be foreseen in the experimental layout.

The double sextupole structure needed for the measurement with $\bar{\text{H}}$'s produced in nested traps or Paul traps typically has a solid angle of $\sim 5 \times 10^{-5} - 10^{-4}$. Assuming that the recently reported production rates can be scaled by the factor 100 higher antiproton trapping efficiency of the ASACUSA RFQD and catching trap, one can expect an event rate at the $\bar{\text{H}}$ detector of about one event per minute during the mixing cycles, enough to make one scan per day. With further improvements of the production process, a high-statistics determination of the resonance shape will be possible.

5.2 The antihydrogen beam line

We plan to adopt a similar method to that of the classic hydrogen experiments. Thus we envisage a beamline in which the antihydrogen atoms pass through *i*) an inhomogeneous magnetic field, which selects their spins and velocities, *ii*) a microwave cavity which induces spin-flip transitions when tuned to ν_{HF} , and *iii*) a second inhomogeneous field which analyzes the state of the spin-flipped atoms. In contrast to the case of hydrogen, the number of antihydrogen atoms which can

be expected is of course sharply limited. To compensate to some extent for this, we make use of sextupole magnet systems since these can accept and transport antihydrogen atoms emerging into a large solid angle.

A schematic view of the whole experimental apparatus is shown in Fig. 3. The two sextupole magnets S1 and S2 are aligned so as to accept antihydrogen atoms emitted transversally from the formation region. The focussing and spin selection in the sextupoles is based on the magnetic field gradient force which acts on the magnetic moment of the antihydrogen atoms. A strong magnetic field gradient will introduce a bend in their trajectory depending on the direction of their alignment with respect to the magnetic field. The four possible hyperfine states of an antihydrogen atom, characterized by the quantum numbers $F = 0, 1$ (total spin) and $M_F = -1, 0, 1$ (projection of F onto the magnetic field axes), then divide into two pairs: the so-called "high-field seekers", which move towards regions of higher magnetic field, and the "low-field seekers" (cf. Fig. 2) which move toward weaker-field regions.

For two identical sextupole magnets, the trajectories shown in Fig. 3 correspond to low-field seekers that do not change their spin direction inside the cavity. A resonant microwave field would transform the low-field seekers into high-field seekers, which would be blocked in S2, and the on-resonance count rate at the antihydrogen detector would drop from a constant rate off-resonance. This kind of "signal disappearance" measurement is not well suited for experiments with low count rates. The signature can be reversed simply by rotating S2 by 180 degrees with respect to S1. This way, the magnetic field directions between the sextupoles are exactly turned by 180 degrees, which will transform low-field seekers into high-field seekers. Thus, low-field seekers passing S1 will only be focussed by S2 if they have undergone a spin-flip inside the cavity.

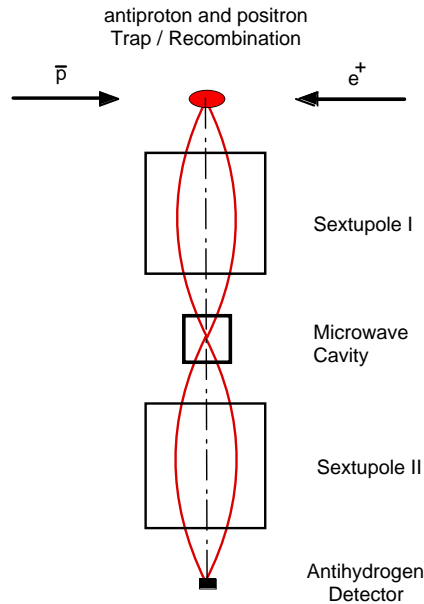


Figure 3: A schematic layout of a simple microwave resonance experiment for antihydrogen. The antihydrogen atoms, which are produced in the central region of a charged particle trap, are transported via a couple of sextupole magnets. Spin selected antihydrogen atoms in the first sextupole magnet enter a microwave cavity and spin-flipped atoms are analyzed in the second magnet.

5.3 Velocity distribution of antihydrogen atoms in the beam

$\bar{\text{H}}$ atoms leaving the formation region move almost freely. The kinetic energy and direction may depend on the condition of recombination, but at the present stage these are not well known.

For the present purpose we assume that the produced antihydrogen atoms follow a Maxwell distribution at the trap temperature T and distribute isotropically. The distribution is give by

$$\Delta N/N = \frac{4}{\pi} v'^2 e^{-v'^2} \Delta v', \quad (20)$$

with $v' = v/v_m$ and $v_m = \sqrt{2kT/m}$. $\Delta N/N$ is the relative number of atoms in the velocity interval between v' and $v' + \Delta v'$. v_m is the most probable velocity, T the temperature of the atom cloud and m the mass of an Antihydrogen atom. Typical Maxwell distributions and mean velocities are given in Fig. 4.

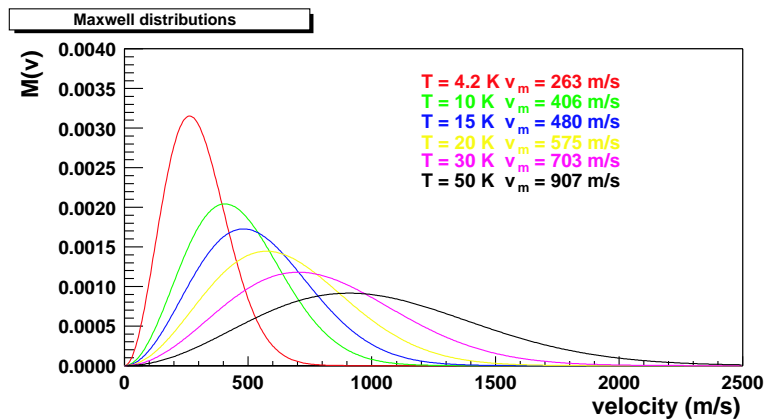


Figure 4: Maxwellian velocity distribution for various temperatures of the produced antihydrogen.

5.4 Antihydrogen beam transport in sextupole fields

The magnetic energy of a hydrogen atom of magnetic moment $\vec{\mu}$ in a magnetic field $\vec{B}(\vec{r})$ is

$$V_{mag} = -\vec{\mu} \cdot \vec{B}. \quad (21)$$

Thus, the neutral atom feels a force

$$\vec{F} = -\text{grad } V = \text{grad } (\vec{\mu} \cdot \vec{B}). \quad (22)$$

If a moving antihydrogen atom experiences changes of the magnetic field \vec{B} that are slow compared to the Larmor frequency, its magnetic moment will adiabatically follow the magnetic field lines, keeping its projection onto them constant. The product $\vec{\mu} \cdot \vec{B}$ will therefore only depend on the *magnitude* of \vec{B} (provided $\vec{\mu}$ is constant), not on its direction.

Sextupole magnets are commonly used to focus neutral atoms. A sextupole field is described by a scalar potential S with form (in polar coordinates r, ϕ, z)

$$S(r, \phi) = C r^3 \sin 3\phi \quad (23)$$

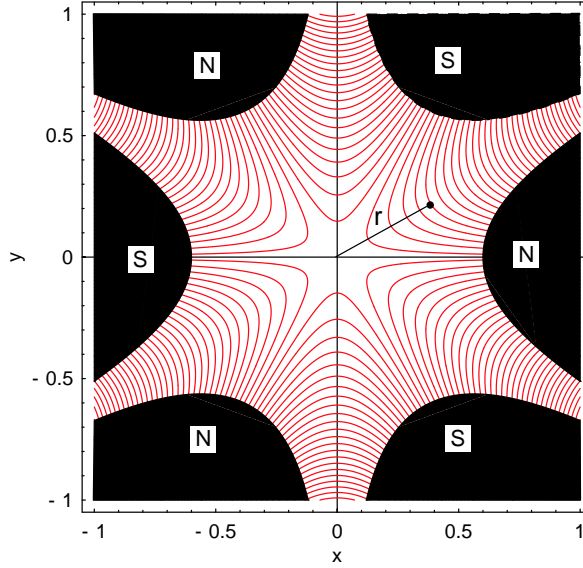


Figure 5: Magnetic field lines (red) of a sextupole magnet. The black parts are the magnet poles which follow an equipotential line. N = north pole, S = south pole.

The magnetic field following from $\vec{B} = -\text{grad } S$ has the Cartesian coordinates $(3Cr^2 \sin 3\phi, 3Cr^2 \cos 3\phi, 0)$. Its magnitude is then simply given by

$$B(r) = 3C r^2 = cr^2, \quad (24)$$

The magnetic field lines of a sextupole field are shown in Fig. 5. They are produced by magnetic poles of alternating polarity shaped as equipotential surfaces of $S(r, \phi)$.

The bending force as defined in Eq. 22 becomes then

$$\vec{F} = \text{grad} (\vec{\mu} \cdot \vec{B}) = \text{grad} (\mu B(r)), \quad (25)$$

which has only a radial component

$$F_r = \mu \frac{\partial B}{\partial r} = 2c\mu r. \quad (26)$$

An antihydrogen atom moving in z direction (perpendicular to the plane shown in Fig 5) with velocity v_z will undergo radial harmonic oscillations with frequency

$$\omega = \sqrt{\frac{2c\mu}{m}}, \quad (27)$$

Thus the focal length l_f of a sextupole is given by the flight time of an atom in z direction corresponding to half an oscillation period in radial direction

$$l_f = \frac{\pi}{\omega} v_z = \pi v_z \sqrt{\frac{m}{2c\mu}}. \quad (28)$$

The double field gradient c is practically limited by the strength of the magnetic field at the pole surface ($r = r_{\max}$). Technically $B_m = 1.2$ T is feasible, so that c is determined by $B(r_{\max}) = B_m = cr_{\max}^2$ or

$$c = B_m / r_{\max}^2. \quad (29)$$

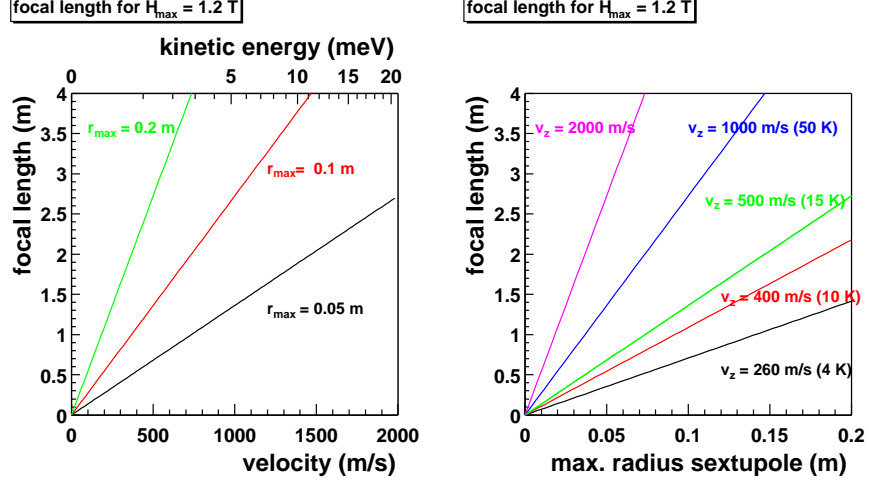


Figure 6: Dependence of the focal length of a sextupole on the atom velocity (left) and sextupole radius (right).

The focal length as function of the three experimental parameters B_m , r_{\max} , and v_z then becomes

$$l_f = \pi v_z r_m \sqrt{\frac{m}{2B_m \mu}}. \quad (30)$$

Fig. 6 shows l_f for typical ranges of the three parameters. Assuming velocities of about 500 m/s corresponding to the mean velocity for a temperature of 15 K, typical sextupole sizes will be 1.25 m length for a radius of 0.1 m, or 2.5 m for a radius of 0.2 m.

5.5 Microwave resonance apparatus

A microwave cavity for 1.42 GHz has typically the dimensions of the corresponding wavelength of 21 cm. As the detailed simulations in section 6 show, it needs openings of a few centimeter diameter for the antihydrogen atoms to enter and leave. A possible solution is a scaled copy of the 12.9 GHz cavity used by our group to measure the hyperfine splitting of antiprotonic helium at the AD [44, 45]. It is a cylindrical cavity oscillating in the TM_{110} mode and would be placed with the cylinder axis parallel to the sextupole axis. Thus the magnetic field strength is independent of the z direction. The 12.9 GHz cavity has two meshes with a transmission of 80% on top and bottom of the cylinder which cover about half of the opening area, and still reaches Q -factors of several 1000. For a resonance frequency of 1.42 GHz, the dimensions would be about 25.7 cm in diameter and a length of 22.3 cm, which would nicely fit in the space between the two sextupoles.

5.6 Resonance line shape and achievable resolution

The microwave field will induce transitions between 2 of the hyperfine states of the atom. The transition probability P_{12} between two stable levels 1, 2 of an atom which spends a time T inside an oscillating magnetic field $B(t) = B_0 e^{-i\omega t}$ can be easily calculated from the time dependent Schrödinger equation and is given in many textbooks [46] as

$$P_{12} = \frac{4b^2}{4b^2 + (\omega - \omega_0)^2} \sin^2 \left[\frac{1}{2} \sqrt{4b^2 + (\omega - \omega_0)^2} T \right] \quad (31)$$



Figure 7: 12.9 GHz cavity used by ASACUSA to measure the hyperfine structure of antiprotonic helium. It has an inner diameter of 28.8 mm, and uses meshes on both top and bottom of the cylinder to let antiprotons and laser beams pass. The microwave radiation is provided by a rectangular wave guide from top, and the magnetic field strength in the cavity is monitored by a pick-up antenna attached below.

with $\hbar\omega_0 = E_2 - E_1$ being the energy difference between the two states and b the transition amplitude which depends on the strength of the oscillating magnetic field B_0 and the transition dipole moment. The probability has a maximum for $bT = \pi/2$, which defines the relation between the cavity length $L = v_z T$ and B_0 . Since the only observable transitions are those flipping the positron spin, the transition dipole moment is of the order of a Bohr magneton. Then, in the case of $v_z \sim 500$ m/s and $L \sim 20$ cm, a magnetic field amplitude of $B_0 \sim 5 \times 10^{-4}$ Gauss is needed.

For a given velocity, the width of $P_{12}(\nu)$ is given by $\delta\nu = 0.799/T$, which for the above parameters yields $\delta\nu = 2.2$ kHz and $\delta\nu/\nu_{\text{HF}} = 1.6 \times 10^{-6}$. The Monte-Carlo simulations for the various experimental layouts show (e.g. Fig. 11) that the velocity distribution after the double solenoid is rather narrow (FWHM ~ 25 m/s for $v = 350$ m/s), so that the final resonance line width will not be significantly broadened. With good enough statistics, the center of the resonance line can easily be determined with a relative precision of 10^{-6} or better.

5.7 Antihydrogen detection

When antihydrogen atoms collide with matter, the annihilation of both antiproton and positron can be used to uniquely identify $\bar{\text{H}}$ atoms. As shown in the following section on the production methods, the double sextupole structure is only transparent to $\bar{\text{H}}$ atoms in the desired spin states. All other $\bar{\text{H}}$ atoms will annihilate around the formation region or inside the sextupoles, and by applying proper shielding, the annihilation products can be kept from reaching the antihydrogen detector region. This way, a detection efficiency of 100% for antihydrogen atoms can be easily obtained without serious background.

6 Antihydrogen Production

6.1 $\bar{\text{H}}$ production in nested Penning traps in a split solenoid magnet

The only proven method for $\bar{\text{H}}$ production is by using nested Penning traps as recently demonstrated by ATHENA [37] and ATRAP [38, 39]. It would therefore be straight forward to use this method also for the proposed measurement of the GS-HFS. However, this production method has several disadvantages:

- **access:** the traps are located inside a superconducting solenoid magnet.
- **source size:** the positron plasma, in which the $\bar{\text{H}}$ formation takes place, has a large size (typically a few centimeters along the solenoid axis and a few millimeters perpendicular to it), which causes large aberrations in the sextupole transport section.
- **plasma rotation:** the positron plasma rotates around the magnetic field axis, which leads to an additional boost to the $\bar{\text{H}}$ atoms.

Nevertheless, as the production parameters and rates are now known, it is a possible scenario also for the proposed experiment.

Experimentally, only the transverse direction is practically possible to extract antihydrogen atoms, because the longitudinal direction (namely, the solenoid axis) is occupied by the devices for incoming antiprotons and positrons. Thus, we need an open space where the produced antihydrogen atoms traverse without obstacle, requiring a split solenoid type configuration for antihydrogen formation. Fig. 8 shows a possible layout of the formation region in a split solenoid. In addition to a split solenoid, the central electrodes have to be made of meshes to allow the neutral atoms to pass. This is not expected to be any serious problem for the performance of the nested traps.

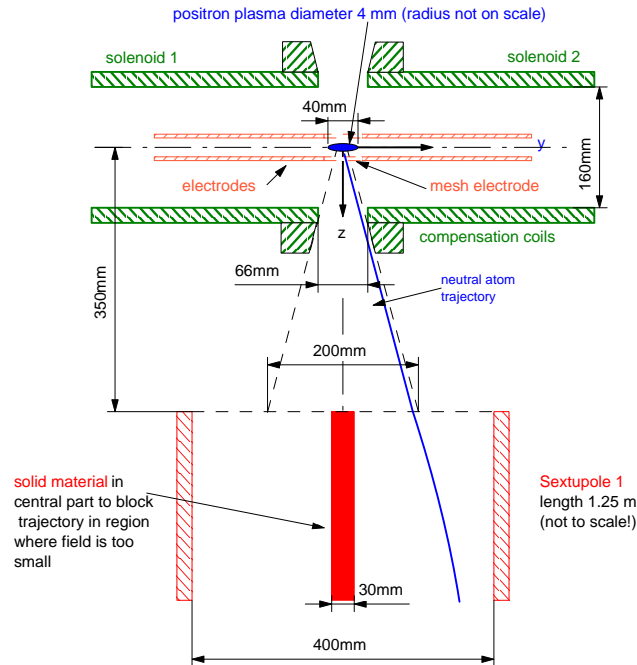


Figure 8: Drawing of the central formation region in a split solenoid.

Table 2: Parameters for $\bar{\text{H}}$ production.

Source parameters	value	comment
internal temperature of plasma clouds	15 K	
rotation frequency of e^+ plasma	100 kHz	for $10^8 e^+/\text{cm}^3$
diameter of e^+ plasma	4 mm	FWHM gaussian
length of e^+ plasma	40 mm	

Additionally the magnetic moment of the antihydrogen atoms has to be taken into account. A strong magnetic field gradient will bend the atoms depending on their alignment with respect to the magnetic field. The four possible hyperfine states of an antihydrogen atom which are characterized by the quantum numbers $F = 0, 1$ (total spin) and $M_F = -1, 0, 1$ (projection of F onto the magnetic field axes) divide into two so-called "high-field seekers" which move towards higher magnetic field and two "low-field seekers" (cf. Fig. 2). If the atoms leave a solenoidal field perpendicular to the field lines, the field gradient points in their direction of motion or against it depending on the quantum numbers, and therefore does not deflect them.

If the kinetic energy of the atoms is lower than their magnetic energy in the magnetic field gradient, the high-field seekers will remain inside the solenoid field and only the low-field seekers escape. In this case automatically there is a selection of the spin direction. For antihydrogens of temperature T the magnitude of magnetic field that can trap is

$$B = 1.3 \text{ Tesla/K.} \quad (32)$$

This means that for $T > 4$ K practically there is no selection of antihydrogen spins when they are emitted from the solenoid.

In order to estimate the event rate, a Monte-Carlo simulation of the trajectories of $\bar{\text{H}}$ atoms of different quantum states was performed. The parameters of the ATHENA experiment [37] (cf. Table 2) were used as a typical example. Fig. 9 shows the resulting velocity distribution of atoms. It is clearly seen that the natural rotation of the plasma does not drastically change the velocity distribution for the plasma parameters used here.

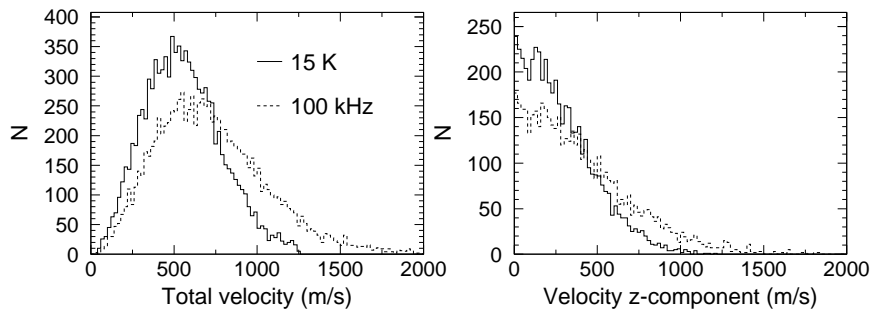


Figure 9: Velocity distribution of $\bar{\text{H}}$ atoms formed in a split solenoid. The solid line corresponds to a Maxwell distribution of $T = 15$ K, and the dashed line shows the velocity distribution if the atoms are formed in a cloud of temperature 15 K that rotates with a frequency of 100 kHz.

The simulation showed, that the large size of the \bar{H} source leads to large aberrations in the sextupoles if they are put too close to the source. This is especially serious since the proposed method requires that the magnetic field direction at the exit of sextupole 1 and in the entrance of sextupole 2 are exactly reversed by 180 degrees. To minimize the aberrations, a rather large distance of 35 cm has to be chosen. To obtain a large enough solid angle, the diameter of the sextupoles has to be increased to 40 cm. The length of the sextupoles was set to 1.25 m so that the resulting total length of 4.5 m just fits into the current ASACUSA area at the AD. Fig. 10 shows the trajectories of atoms in different quantum states. It is clearly seen that no atoms in wrong states or those whose spin has not been flipped in the cavity arrive at the hydrogen detector, so that no background exists for the detection of \bar{H} atoms except of pions from \bar{p} 's annihilating inside the sextupoles. They can be eliminating by proper shielding. The optimization of the shielding is straight forward and will be performed by GEANT simulations once a configuration has been chosen.

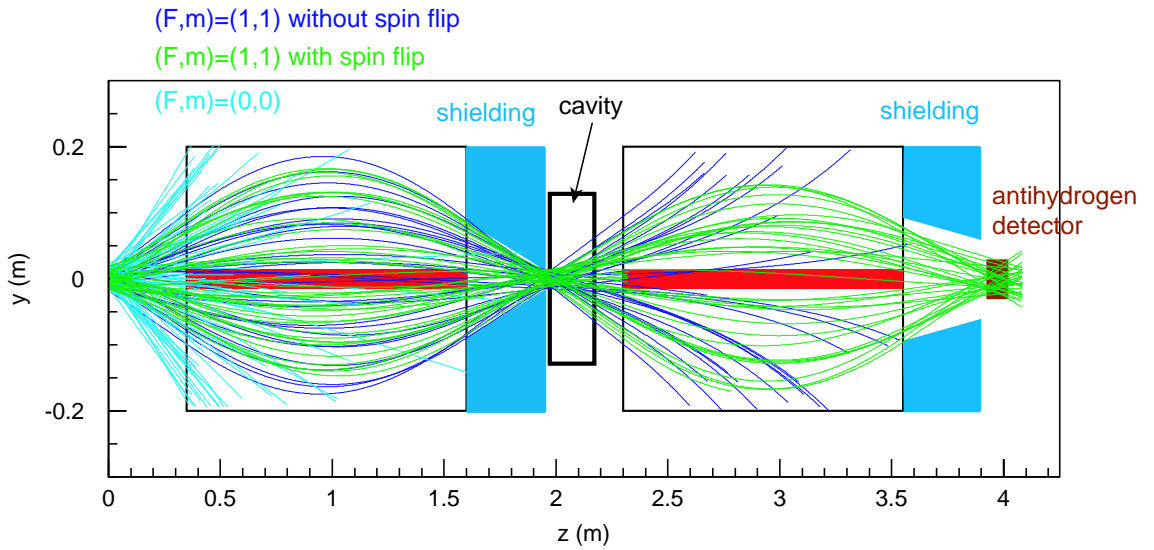


Figure 10: Trajectories of atoms in different spin states. The total length of about 4.5 m is chosen so that the whole setup just fits into the current ASACUSA area at the AD.

In Fig. 11 the velocity distribution of antihydrogen atoms that reach the detector is plotted. It shows that the double sextupole setup has only a narrow acceptance in velocity space. Therefore the actual dimensions of the sextupoles do not matter so much, different configurations will only cut out different slices from the original velocity distribution. On the other hand, by varying the magnetic field, the velocity distribution of formed \bar{H} can be measured.

For the shown configuration, the transmission is $\epsilon = 4 \times 10^{-4}$, i.e. of all formed antihydrogen atoms of the $(F, m) = (1, 1)$ state, the fraction ϵ reaches the \bar{H} detector. Since the background is very low, and antihydrogen annihilation can easily be detected with 100% efficiency, there is no loss in the detection process. Out of all states formed, the low-field seeker constitute only 50%. Furthermore, due to aberrations we may lose another estimated factor 2–4, so that on resonance we expect fractions between 5×10^{-5} and 2×10^{-4} of the atoms to arrive at the \bar{H} detector. Taking the observed production rate of ATHENA and scaling it with the factor 100 more efficient trapping demonstrated by ASACUSA using our RFQD, we can expect a production rate of $\sim 200 \bar{H}/s$, yielding a count rate on resonance of about 0.5 – 2.5 events/minute.

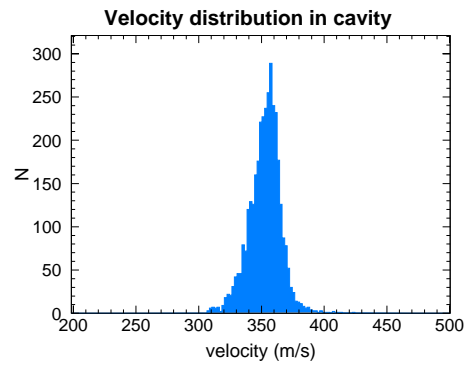


Figure 11: Velocity distribution inside the microwave cavity for those \bar{H} which were detected after S2, .

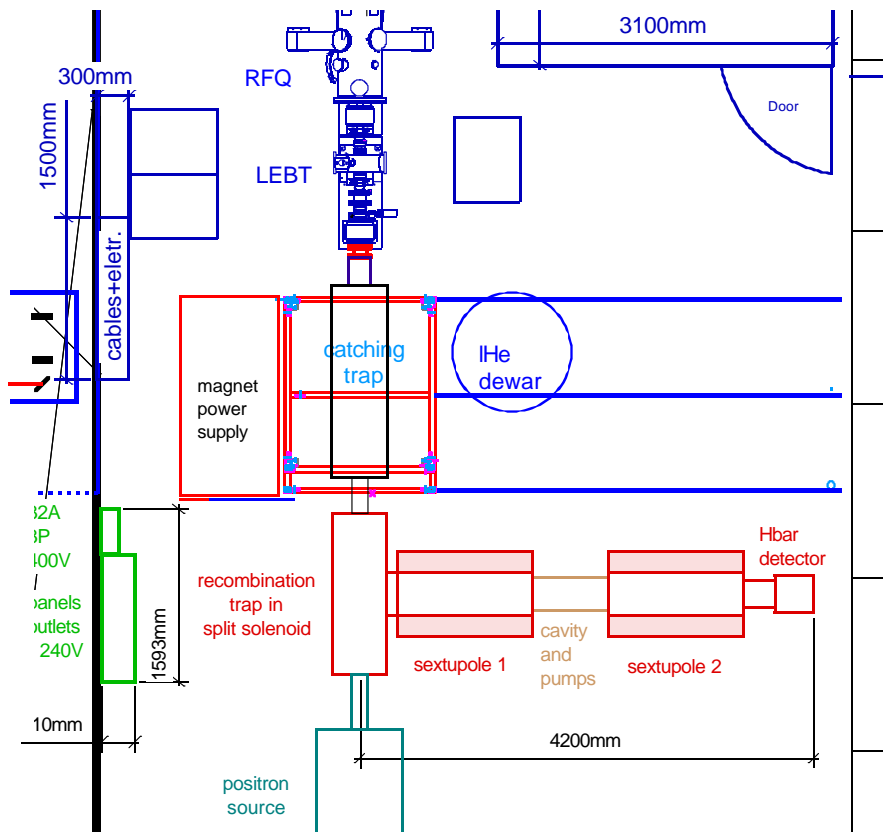


Figure 12: Schematic layout of the split solenoid and sextupole magnets in the current ASACUSA area at the AD.

6.2 $\bar{\text{H}}$ production in radio frequency Paul traps

In this section we describe a new method for producing cold antihydrogen atoms in a region of zero applied DC magnetic field, and in numbers adequate for the GS-HFS experiment discussed above. While existing experiments produce antihydrogen atoms [37–39] in Penning traps, we plan to use a variant of the radio-frequency Paul trap [47]. Since RF traps require no superconducting solenoids, they are far more compact than Penning traps. The proposed design has 2–4 openings, each of solid angle $\sim 5\% \times 4\pi$, through which antihydrogen atoms, once formed, can emerge into the sextupole beam line described elsewhere in this LOI. Moreover, high-precision spectroscopic studies of these emerging antihydrogen atoms are all the more easily made because they are not subject to the perturbing influence of the strong magnetic fields present in Penning traps.

In Fig. 13, a plan view of the proposed experimental layout is shown. The setup consists of i) the radio-frequency quadrupole decelerator (RFQD) currently installed in the ASACUSA beamline of the AD, ii) the antihydrogen source described below, and iii) the sextupole magnets and radio-frequency cavities making up the atomic beam line to be used for GS-HFS measurements of antihydrogen atoms emitted from the source.

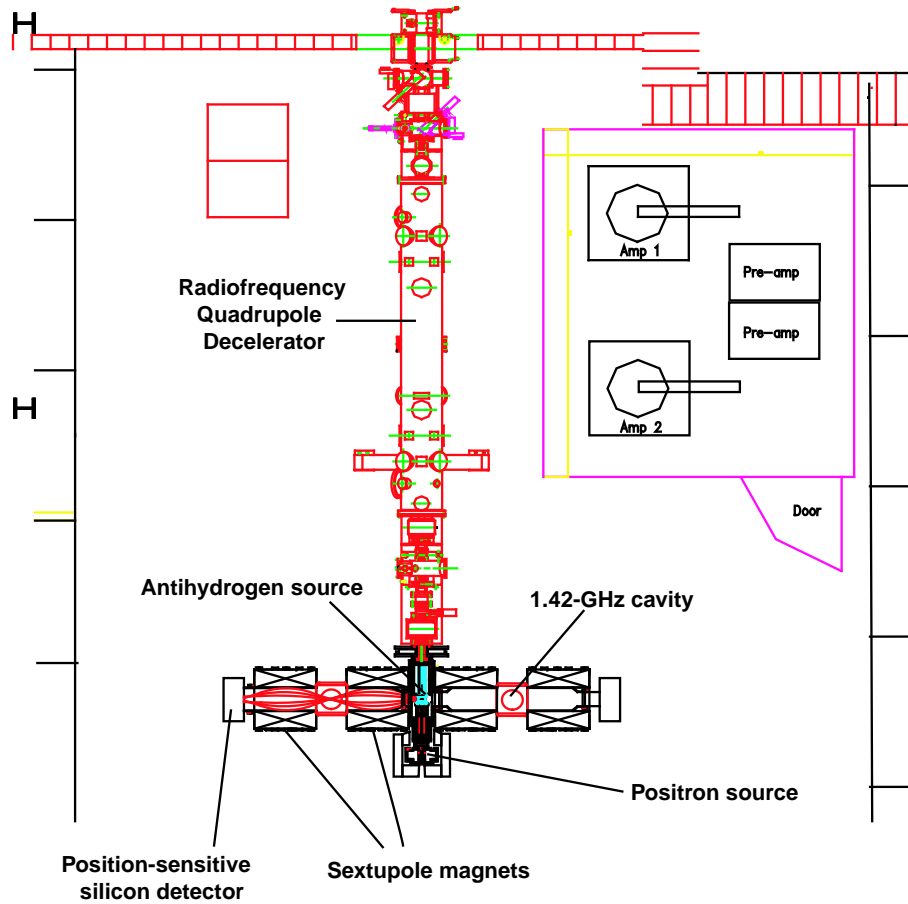


Figure 13: Top view of proposed antihydrogen experiment, including spectrometer for HFS spectroscopy.

6.2.1 Experimental apparatus and methods

A detailed cross-sectional view of the antihydrogen source is shown in Fig. 14. It consists of three adjacent Paul traps. The left is used to trap antiprotons (\bar{p} catching trap), and the right one will trap positrons (e^+ catching trap'). In the central trap ('recombination trap'), the two particle species are mixed together to produce the antihydrogen atoms. The three traps are to be placed in an ultra-high vacuum chamber of length $l < 1$ m and will be cryogenically cooled to $T = 5$ K to reach a residual pressure of $P < 10^{-13}$ mbar. This pressure corresponds to an antiproton lifetime, τ , against annihilation on residual gas molecules of about ~ 1 hour. Similar vacuum and cryogenic requirements [48] have already been achieved at the AD by the ATRAP, ATHENA, and ASACUSA experiments. All three traps will be superconducting (probably using niobium as the superconductor). Strong RF fields can thus be sustained to confine the antiprotons and positrons, with minimal power dissipation.

As already demonstrated in ASACUSA's previous experiments [49], pulsed AD beams containing 2×10^7 antiprotons with energy $T = 5.3$ MeV will be decelerated to $T = 100$ keV by the RFQD, then focused by two solenoid magnets and decelerated to 5 keV by a 1-micron-thick Mylar foil. The antiprotons will then enter a 300-mm-long, 30-mm-diam radio-frequency linear Paul trap [50] driven at a RF frequency of $f \sim 40$ MHz. As each pulse enters the trap, its spatial profile will be

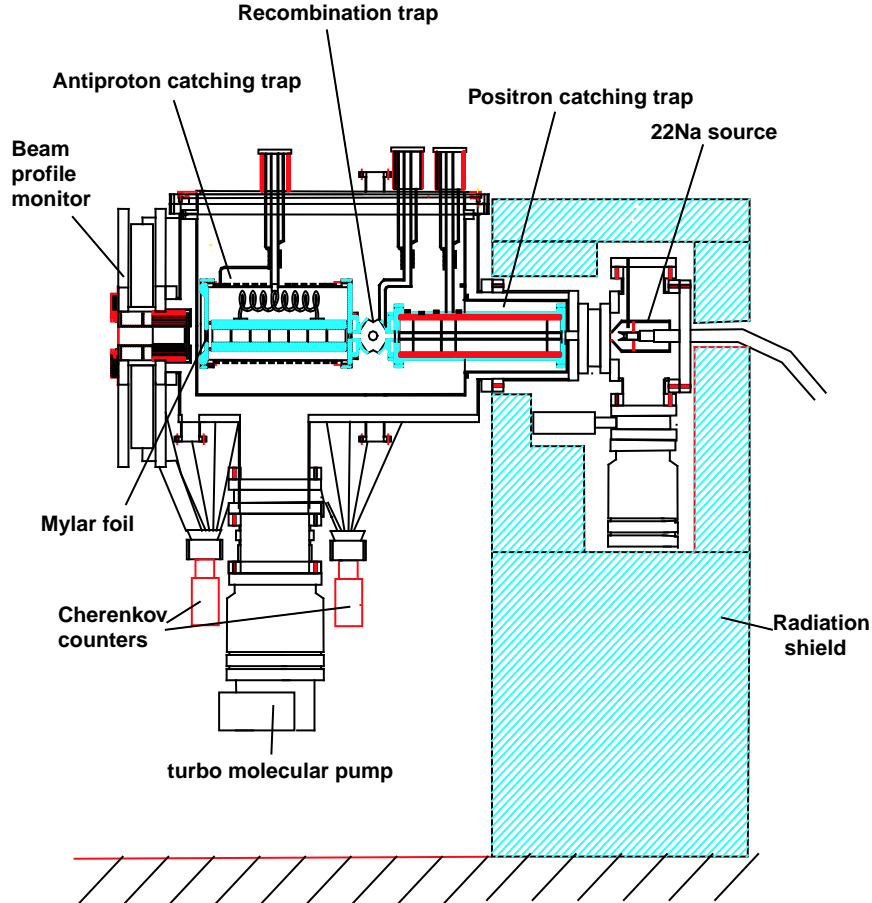


Figure 14: Cross-sectional view of the antiproton, positron, and antihydrogen recombination traps.

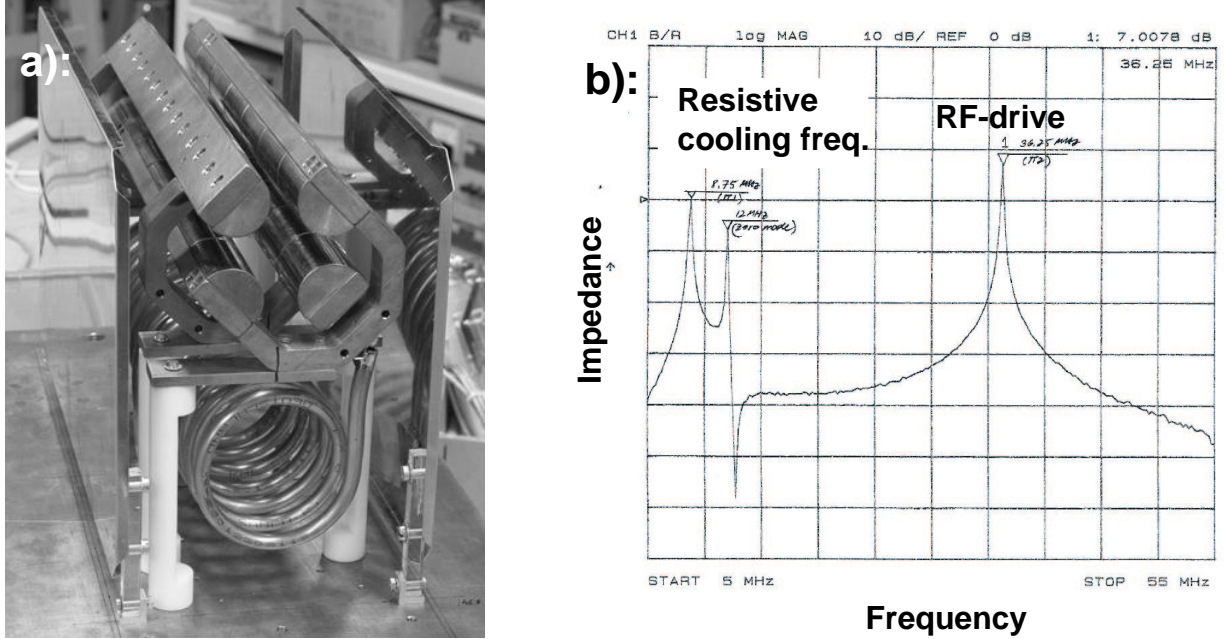


Figure 15: Model of linear Paul trap for antiproton capture and cooling (a). Two RF resonances of the trap model, measured using a vector network analyzer. These correspond to the radio-frequencies used for confining the antiprotons and applying the resistive cooling (b).

measured by a secondary electron microwire profile monitor [51], while its time profile and intensity will be measured by Lucite Cherenkov counters [52]. Simulations based on the expected RF field in the trap, and the known characteristics of the antiproton beam show that about 10^6 antiprotons will be captured per typical pulse. Similar Paul traps and RFQ's have been used for many years in radioactive beam facilities at CERN, GSI [53], GANIL, KEK, NSCL, and other places to capture high-energy ions and cool them.

Once the antiprotons are inside the \bar{p} catching trap, their energy T will be decreased from 5 keV to less than 0.1 eV by resistive cooling [54–57] applied for an estimated period of 100 s. In this cooling technique, the trap electrodes are connected to an external LC circuit whose resonance frequency is tuned to the characteristic secular motion frequency of the antiprotons (typical value $f \sim 10$ MHz). The movement of the particles will induce an electric current through the circuit, thereby dissipating their kinetic energy in a resistor. In past experiments, some 10^4 protons have been confined in a Paul trap and cooled to $T = 900$ K [55] using this technique.

Computer simulations of the RF field have been used to build a realistic model of the proposed linear Paul trap for antiprotons (Fig. 15 (a)). Measurements on its RF characteristics (Fig. 15 (b)) show that the trap structure indeed has both the correct RF resonance frequency to confine the antiprotons, and the LC resonance circuit characteristics to cool them. Beam-dynamics simulations show that these RF fields will compress the antiproton cloud onto the axis of the trap, permitting them to be extracted as a pulsed beam of very low energy (~ 1 eV) and angular divergence.

A pulsed beam of positrons produced in an external source (such as those described elsewhere in this LOI) will be injected into the second linear Paul trap shown in Fig. 14. The e^+ catching trap is $l = 400$ mm long, with a diameter of $d = 20$ mm and a RF drive frequency of ~ 1 GHz. Alternatively, positrons produced from a sodium-22 source can be directly loaded into the trap. The positron cloud will be cooled resistively with an estimated time constant of $\tau \sim 0.1$ s, and

compressed both longitudinally and transversely.

6.2.2 $\bar{\text{H}}$ formation procedure

In the time between two AD shots (100 s), the following sequence will be repeated 5–10 times: After compression, $\sim 10^5$ positrons will be transported into a parabolic recombination Paul trap [47, 55] with diameter $d = 5$ cm, and confined there by the trap fields. Some $\sim 10^4$ – 10^5 antiprotons out of the 10^6 $\bar{\text{p}}$'s stored in the $\bar{\text{p}}$ catching trap will also be captured in the same manner. Beam-optics simulations have shown that particle clouds can be transported from the linear Paul traps to the recombination trap with a high efficiency, provided they are longitudinally compressed beforehand. The loading of Paul traps by pulsed ion beams has already been established experimentally [58–60], and we expect a transfer efficiency of the order 10% from the catching traps to the recombination trap. Although it has been demonstrated [61] that large numbers (density $\rho \sim 10^7$ cm $^{-3}$) of oppositely charged Tl^+ and I^- ions have been simultaneously confined in a trap of design similar to the recombination trap, this has not, to our knowledge, yet been done with electrons and protons. However, according to our extensive simulations, simultaneous trapping of antiprotons and positrons is indeed possible in a Paul trap if this is driven at two frequencies, one in the gigahertz range (for the positrons), the other in the megahertz range (for the antiprotons).

The same simulations show that RF fields will compress the two clouds into an overlap volume with a diameter of a few millimeters at the centre of the trap. Positrons can then be cooled resistively at rates of order $\gamma \sim 10$ – 100 s $^{-1}$, as Dehmelt [54] and Schwinberg [62] have shown for electrons and positrons. Antiprotons will also be resistively cooled using a separate LC circuit at rates $\gamma \sim 0.1$ – 1 s $^{-1}$. The positrons will furthermore dissipate some of their energy by emitting synchrotron radiation in the RF field. As a result of these cooling mechanisms, the particle temperatures will fall to $T < 100$ K, producing antihydrogen atoms in a point-like region in the trap centre. These, being no longer confined by the trap fields, will travel outwards, leave the trap through holes subtending a solid angle of $5\% \times 4\pi$ cut in the electrodes, and enter the GS-HFS sextupole beam line. After the antiprotons and positrons have all recombined (a process expected to take 10–60 s from the instant the two particle species enter the recombination trap), new pulses will be injected and the process repeated. In this manner, we expect to produce antihydrogen atoms almost continuously, at a rate of 10^4 – 10^5 /min.

The antiprotons and positrons must be cooled to temperatures $T < 100$ K in the strong RF field of the Paul trap, in order to produce antihydrogen efficiently. This cooling presents the greatest technical difficulty in this proposal. Now in recent experiments [63], plasmas containing $\sim 10^5$ Mg^+ ions confined in a linear Paul trap have been laser-cooled to produce ionic crystals. Similarly, crystalline ion beams have been produced by laser-cooling Mg^+ ions circulating in a radio-frequency quadrupole storage ring [64]. These experiments were made at particle temperatures far lower than those required in the present proposal. At the same time, 10^4 protons have been cooled resistively to temperatures $T \sim 900$ K in parabolic Paul traps, as described above [55]. Generally, the particle temperatures are determined by the equilibrium between the rate of cooling (laser, resistive, or otherwise), and the heating due to the oscillating RF field (“RF-heating”) [65, 66]. Simulations and experiments show that the particle temperature is strongly dependent on the strength of the RF field, and the number of particles in the trap [67]. We intend to decrease the temperature of the antiprotons to $T < 100$ K first by using a Paul trap with a larger volume and smaller RF field than previously used, and second by increasing the resistive cooling rate by several orders of magnitude [68], with high-Q superconducting LC circuits.

6.2.3 Feasibility tests to be done at CERN and their requirements

The Paul traps will be built by the ASACUSA collaboration. All aspects of their operation, particularly the cooling, must be extensively tested and optimized using protons and electrons before proceeding to experiments involving antiprotons and positrons. To make these feasibility tests, we require a pulsed proton beam with characteristics similar to those of the antiproton beam produced by the ASACUSA-RFQD; namely, energy $T = 60\text{-}100$ keV, pulse-length $\Delta t \sim 100$ ns, and intensity 10^7 particles/pulse. During the construction of the ASACUSA-RFQD in 1999, the CERN duoplasmatron source located in Bat. 152 was used for test purposes. We request the use of this facility for several months between the years 2003–2004. The associated manpower and material costs will be provided by the collaboration.

With the latter proviso concerning manpower and materials, we also request occasional technical assistance and advice from the CERN cryogenics laboratory, and consultations with CERN experts on superconducting cavities. We will also need to be able to use some CERN workshop and laboratory facilities in manufacturing some of the technically difficult parts of the RF Paul traps, particularly those pertaining to superconducting cavities.

6.3 Synthesis of a polarized \bar{H} beam with a cusp trap

A conceptually new and possibly quite effective scheme to synthesize a polarized antihydrene beam is described in this section [69].

The new scheme employs a superposition of a quadrupole magnetic field (cusp field) and an octupole electric field. A schematic configuration is shown in Fig. 16. It is known that the magnetic cusp is strong against magnetohydrodynamic instabilities [70] although charged particles escape along the magnetic field lines. In the case of non-neutral plasmas, particle losses along the magnetic field line is suppressed by the octupole electric field. By this way, the present cusp trap possesses superior characteristics of plasma stability as well as particle confinement of non-neutral plasma. The equilibrium of the positron cloud in the cusp trap along the magnetic field line requires the balance between three forces, i.e., the repulsive force induced by the space charge of the positrons, the electric field of the octupole field, and the force $-|\vec{\mu}_\ell| \nabla |\vec{B}|$, where $\vec{\mu}_\ell$ is the orbital magnetic moment of the positrons. Actually, this third force allows to confine excess positrons beyond the octupole field and as a result induces an attractive force for antiprotons into the cusp trap. As a result, particles with opposite charges can self-stabilized with the positron cloud in the cusp trap, which never happens for the nested trap scheme. This supreme configuration has already been proved to have a high ability to stably confine electron plasma as shown in Fig 16 (b) [71], the confinement time of which is proportional to the square of the magnetic field strength. For the antihydrogen synthesis, a cusp trap with a magnetic field around 3.5 T is under preparation, which will yield a confinement time as long as a couple of hours, which should be long enough for

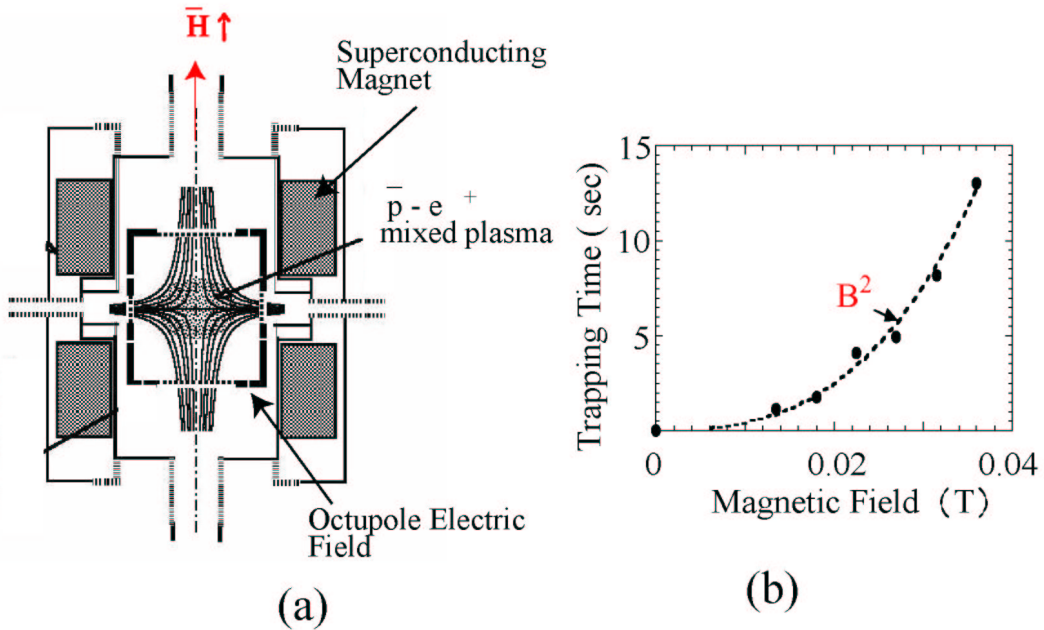


Figure 16: (a) Schematic diagram of the cusp trap superposed consisting of two co-axial superconducting solenoids and electrodes for an octupole electric field generation. Positrons and antiprotons are stably confined at the central part of the trap simultaneously resulting in a spontaneous antihydrogen formation. (b) The trapping time of electron in a prototype cusp trap as a function of the magnetic field strength.

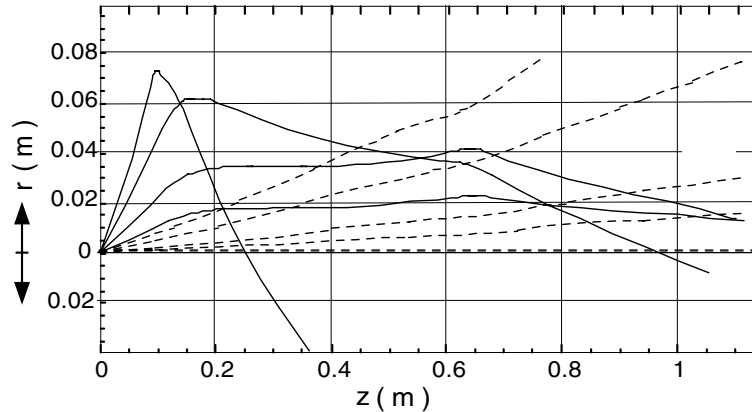


Figure 17: Examples of antihydrogen trajectories emitted at 5, 10, 20 and 30 degrees around 4 K in the low-field-seeking state (solid lines) and the high-field-seeking state (dashed lines). z stands for the symmetry axis of the cusp trap, r for the radial direction.

the present purpose. Another important function of the strong magnetic field is to cool positrons via synchrotron radiation, which eventually sympathetically cools antiprotons. Antiprotons so cooled are automatically accumulated around the minimum potential area, i.e., a cold neutral plasma consisting of antiprotons and positrons is formed near the center of the cusp trap, where synthesized antihydrogen atoms emerge. The vacuum chamber is cooled down to the liquid helium temperature with a cryostat, which allows to prepare antiprotons and positrons at several K. The auto co-existence of cold antiprotons and positrons naturally leads them to be combined into antihydrogen via radiative and/or three body recombination processes.

Further, the cusp magnetic field also works as a spin filter and a focusing device. A couple of examples of antihydrogen trajectories are shown in Fig 17 for a reasonable magnetic field configuration. It is seen that a considerable fraction of antihydrogen in the low-field-seeking states are selectively focused at ~ 1 m from the cusp trap. The resultant polarization degree is expected to be as high as 99%. The focusing effect enhances the antihydrogen intensity by a factor of 30. Because this focusing and spin selection is made very close to the the area of antihydrogen production, both the focusing elements and the spin selector can be quite small, which improves the feasibility of the experiment. The cusp trap is combined with MUSASHI (Monoenergetic Ultra Slow Antiproton Source for High-precision Investigations) which had already trapped and cooled several million antiprotons stably and with the high efficient UHV positron accumulator developed by RIKEN (see section 7) [72].

7 Positron production

Positrons are one of the ingredients for antihydrogen production. Their production from ^{22}Na sources is a well-known and often used technique. For an efficient cooling of \bar{p} with positrons a large number of trapped positrons is beneficial. For a typical number of $N_{\bar{p}} = 10^6$ as routinely trapped in the ASACUSA catching trap, a number of $10^7 - 10^8$ positrons will be needed. This can be achieved in several ways. The Atomic Physics Laboratory of RIKEN for instance has built a positron source [72] (cf. Fig. 18) using an electron plasma to slow down the positrons. It is expected to be capable of accumulating about 10^7 positrons per minute in a UHV environment. The largest rate of accumulated positrons so far has been achieved by ATHENA [73] using the buffer-gas accumulation scheme developed by the group of C. Surco in San Diego [74, 75]. A third approach using a Paul trap is described in section 6.2.

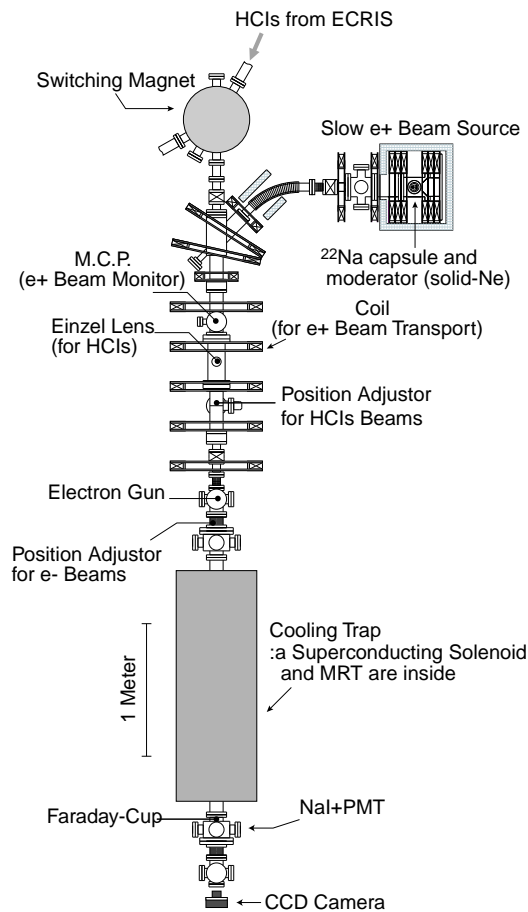


Figure 18: Positron source at the Atomic Physics Laboratory of RIKEN.

8 Technical milestones

We plan to proceed with our development work as follows:

- 2003**
 - design and construction of \bar{p} RF catching trap.
 - design and construction of recombination RF trap.
 - start of experiments with cusp trap.
 - design and fabrication of 1.4 GHz cavity.
- 2004**
 - first test of catching and cooling of protons.
 - construction of recombination RF trap.
 - transfer of protons into recombination RF trap.
 - simultaneous trapping of protons and electrons in RF trap.
 - design of positron accumulator.
 - simultaneous trapping of protons and electrons in cusp trap.
 - **choice of \bar{H} production mechanism**
- 2005**
 - construction of positron accumulator
 - installation of \bar{p} and e^+ traps in the AD hall
 - construction of antihydrogen beam line
 - test of antihydrogen beam line and 1.4 GHz cavity with hydrogen.
- 2006**
 - capture and cooling of antiprotons
 - simultaneous trapping of \bar{p} and e^+
 - recombination studies
 - determination and optimization of \bar{H} parameters (quantum state, velocity)
- 2007**
 - installation of antihydrogen beam line
 - recombination studies
 - determination and optimization of \bar{H} parameters (quantum state, velocity), laser stimulated recombination if necessary
 - **first attempts to measure ν_{HF}** if recombination successful
- 2008**
 - systematic measurements of ν_{HF}

References

- [1] M. Niering et al., Phys. Rev. Lett. 84 (2000) 5496.
- [2] J. R. Sapirstein and D. R. Yennie, Theory of hydrogenic bound states, in *Quantum Electrodynamics*, edited by T. Kinoshita, pages 560–672, World Scientific, Singapore, 1990.
- [3] K. Pachucki, 2003, private communication.
- [4] S. R. Lundeen and F. M. Pipkin, Phys. Rev. Lett. 46 (1981) 232.
- [5] K. Pachucki, D. Leibfried, M. Weitz, A. Huber, W. König, and T. W. Hänasch, J. Phys. B: At. Mol. Opt. Phys. 29 (1997) 177.
- [6] H. Hellwig et al., Proc. IEEE Trans. IM-19 (1970) 200.
- [7] L. Essen, R. W. Donaldson, M. J. Bangham, and E. G. Hope, Nature 229 (1971) 110.
- [8] S. G. Karshenboim, Phys. Lett A 225 (1997) 97.
- [9] M. S. Fee et al., Phys. Rev. A 48 (1993) 192.
- [10] M. Hori, J. Eades, E. Widmann, H. Yamaguchi, J. Sakaguchi, T. Ishikawa, R. S. Hayano, H. A. Torii, B. Juhász, D. Horváth, and T. Yamazaki, Phys. Rev. Lett. 87 (2001) 093401.
- [11] K. Hagiwara et al., Physical Review D 66 (2002) 010001.
- [12] R. S. van Dyck, P. B. Swinberg, and G. Dehmelt, Phys. Rev. Lett. 59 (1987) 26.
- [13] G. G. Simon, C. Schmitt, F. Borokowski, and V. Walther, Nucl. Phys. A 333 (1980) 381.
- [14] N. Ramsey, Atomic hydrogen hyperfine structure experiments, in *Quantum Electrodynamics*, edited by T. Kinoshita, pages 673–695, World Scientific, Singapore, 1990.
- [15] I. I. Rabi, J. M. B. Kellogg, and J. R. Zacharias, Phys. Rev. 46 (1934) 157.
- [16] I. I. Rabi, J. M. B. Kellogg, and J. R. Zacharias, Phys. Rev. 46 (1934) 163.
- [17] J. M. B. Kellogg, I. I. Rabi, and J. R. Zacharias, Phys. Rev. 50 (1936) 472.
- [18] J. E. Nafe and E. B. Nelson, Phys. Rev. 73 (1948) 718.
- [19] A. G. Prodell and P. Kusch, Phys. Rev. 88 (1952) 184.
- [20] H. M. Goldenberg, D. Kleppner, and N. F. Ramsey, Phys. Rev. Lett. 8 (1960) 361.
- [21] C. Cesar et al., Phys. Rev. Lett. 77 (1996) 255.
- [22] A. G. Martin, K. Helmerson, V. S. Bagnato, G. P. Lafyatis, and D. E. Pritchard, Phys. Rev. Lett. 61 (1988) 2431.
- [23] K. Helmerson, A. G. Martin, and D. E. Pritchard, J. Opt. Soc. Am. B 9 (1992) 483.
- [24] A. Kreissl, A. D. Hancock, H. Koch, T. Köhler, H. Poth, U. Raich, D. Rohmann, A. Wolf, L. Tauscher, A. Nilsson, M. Suffert, M. Chardalas, S. Dedoussis, H. Daniel, T. von Egidy, F. J. Hartmann, W. Kanert, H. Plendl, G. Schmidt, and J. J. Reidy, Z. Phys. C 37 (1988) 557.

- [25] D. Colladay and V. A. Kostelecky, *Phys. Rev. D* 55 (1997) 6760.
- [26] R. Bluhm, V. A. Kostelecky, and N. Russell, *Phys. Rev. Lett.* 79 (1997) 1432.
- [27] R. Bluhm, V. A. Kostelecky, and N. Russell, *Phys. Rev. D* 57 (1998) 3932.
- [28] V. A. Kostelecky, *Phys. Rev. Lett.* 80 (1998) 1818.
- [29] R. Bluhm, V. A. Kosteleck, and N. Russell, *Phys. Rev. Lett.* 82 (1999) 2254.
- [30] G. Gabrielse, A. Khabbaz, D. S. Hall, C. Heimann, H. Kalinowsky, and W. Jhe, *Phys. Rev. Lett.* 82 (1999) 3198.
- [31] H. Dehmelt, R. Mittleman, R. S. Van Dyck, Jr., and P. Schwinberg, *Phys. Rev. Lett.* 83 (1999) 4694.
- [32] R. K. Mittleman, I. I. Ioannou, H. G. Dehmelt, and N. Russell, *Phys. Rev. Lett.* 83 (1999) 2116.
- [33] D. Bear, R. E. Stoner, R. L. Walsworth, V. A. Kostelecky, and C. D. Lane, *Phys. Rev. Lett.* 85 (2000) 5038.
- [34] D. F. Phillips, M. A. Humphrey, E. M. Mattison, R. E. Stoner, R. F. C. Vessot, and R. L. Walsworth, *Phys. Rev. D* 63 (2001) 111101.
- [35] V. W. Hughes, M. G. Perdekamp, D. Kawall, W. Liu, K. Jungmann, and G. Putlitz, *Phys. Rev. Lett.* 87 (2001) 111804.
- [36] J. M. Link et al. (FOCUS collaboration), *Phys. Lett. B* 556 (2003) 7.
- [37] M. Amoretti, C. Amsler, G. Bonomi, A. Bouchta, P. Bowe, C. Carraro, C. L. Cesar, M. Charlton, M. J. T. Collier, M. Doser, V. Filippini, K. S. Fine, A. Fontana, M. C. Fujiwara, R. Funakoshi, P. Genova, J. S. Hangst, R. S. Hayano, M. H. Holzscheiter, L. V. Jrgensen, V. Lagomarsino, R. Landua, D. Lindelf, E. L. Rizzini, M. Macr, N. Madsen, G. Manuzio, M. Marchesotti, P. Montagna, H. Pruyss, C. Regenfus, P. Riedler, J. Rochet, A. Rotondi, G. Rouleau, G. Testera, A. Variola, T. L. Watson, and D. P. Van Der Werf, *Nature* 419 (2002) 456.
- [38] G. Gabrielse, N. S. Bowden, P. Oxley, A. Speck, C. H. Storry, J. N. Tan, M. Wessels, D. Grzonka, W. Oelert, G. Schepers, T. Sefzick, J. Walz, H. Pittner, T. W. Hänsch, and E. A. Hessels, *Phys. Rev. Lett.* 89 (2002) 213401.
- [39] G. Gabrielse, N. S. Bowden, P. Oxley, A. Speck, C. H. Storry, J. N. Tan, M. Wessels, D. Grzonka, W. Oelert, G. Schepers, T. Sefzick, J. Walz, H. Pittner, T. W. Hänsch, and E. A. Hessels, *Phys. Rev. Lett.* 89 (2002) 233401.
- [40] G. Gabrielse, S. L. Rolston, L. Haarsma, and W. Kells, *Phys. Lett. A* 129 (1988) 38.
- [41] R. Landua, talk given at the International Workshop on Exotic atoms - future perspectives, Vienna, November 28-30, 2002.
- [42] A. Wolf, *Hyperfine Interactions* 76 (1993) 198.
- [43] A. Müller and A. Wolf, *Hyperfine Interactions* 109 (1997) 233.

- [44] ASACUSA collaboration, Atomic spectroscopy and collisions using slow antiprotons, CERN/SPSC 97-19, CERN/SPSC 2000-04, 1997/2000.
- [45] E. Widmann, J. Eades, T. Ishikawa, J. Sakaguchi, T. Tasaki, H. Yamaguchi, R. S. Hayano, M. Hori, H. A. Torii, B. Juhász, D. Horváth, and T. Yamazaki, *Phys. Rev. Lett.* 89 (2002) 243402.
- [46] P. Kusch and V. W. Hughes, Atomic and molecular beam spectroscopy, in *Encyclopedia of Physics Vol. XXXVII/1*, pages 1–172, Springer, Berlin, 1959.
- [47] W. Paul, *Rev. Mod. Phys.* 62 (1990) 531.
- [48] G. Gabrielse, *New Scientist* 158 (1998) 51.
- [49] See status report of ASACUSA accompanying this LOI.
- [50] J. D. Prestage, G. J. Dick, and L. Maleki, *J. Appl. Phys.* 66 (1989) 1013.
- [51] M. Hori, to be submitted to *Nucl. Instr. Meth. Phys. Res. A*.
- [52] M. Hori, K. Yamashita, R. S. Hayano, and T. Yamazaki, *Nucl. Instr. Meth. Phys. Res. A* 496 (2003) 102.
- [53] W. Quint et al., *Hyperfine Interactions* 132 (2001) 457.
- [54] H. G. Dehmelt and F. L. Walls, *Phys. Rev. Lett.* 21 (1968) 127.
- [55] D. A. Church and H. G. Dehmelt, *J. Appl. Phys.* 40 (1969) 3421.
- [56] D. J. Wineland and H. G. Dehmelt, *J. Appl. Phys.* 46 (1975) 919.
- [57] L. S. Brown and G. Gabrielse, *Rev. Mod. Phys.* 58 (1986) 233.
- [58] M. Kishore and P. Ghosh, *Int. J. Mass Spectrom. Ion Phys.* 29 (1979) 345.
- [59] C.-S. O and H. Schuessler, *Int. J. Mass Spectrom. Ion Phys.* 40 (1981) 53, *J. Appl. Phys.* 52 (1981) 1157.
- [60] R. B. Moore and G. Rouleau, *J. Mod. Optics* 39 (1992) 361.
- [61] J. P. Schermann and F. G. Major, *Appl. Phys.* 16 (1978) 225.
- [62] P. B. Schwinberg, R. S. Van Dyck Jr., and H. G. Dehmelt, *Phys. Lett.* 81 (1981) 119.
- [63] M. Drewsen et al., *Phys. Rev. Lett.* 81 (1998) 2878.
- [64] T. Schätz, U. Schramm, and D. Habs, *Nature* 412 (2001) 717.
- [65] R. Blümel, C. Kappler, W. Quint, and H. Walther, *Phys. Rev. A* 40 (1989) 808.
- [66] R. Blümel, *Phys. Rev. A* 51 (1995) 620.
- [67] Y. Maeno, M. Tachikawa, Y. Moriwaki, and T. Shimizu, *Jpn. J. Appl. Phys.* 34 (1995) L174.
- [68] E. A. Cornell et al., *Phys. Rev. Lett.* 63 (1989) 1674.
- [69] A. Mohri and Y. Yamazaki, submitted to *Europhysics Lett.*

- [70] J. Berkowitz, H. Grad, and H. Rubin, in *Proc. Second United Nations Conf. on the Peaceful Uses of Atomic Energy, Vol. 31*, pages 177–189, United Nations, Geneva, 1958.
- [71] A. Mohri, T. Yuyama, Y. Kiwamoto, Y. Yamazawa, and T. Michishita, *Jpn. J. Appl. Phys.* 37 (1998) L1553, A. Mohri, private communication.
- [72] N. Ohshima, T. M. Kojima, M. Niigaki, A. Mohri, K. Komaki, and Y. Yamazaki, *Nucl. Instrum. Methods B*, in press.
- [73] D. P. van der Werf, L. V. Jorgensen, T. L. Watson, M. Charlton, M. J. T. Collier, M. Doser, and R. Funakoshi, *Appl. Surf. Sci.* 194 (2002) 312.
- [74] T. J. Murphy and C. M. Surko, *Phys. Rev. A* 46 (1992) 5696.
- [75] R. G. Greaves, M. D. Tinkle, and C. M. Surko, *Phys. Plasmas* 1 (1994) 1439.